

Cylindrical Lens by a Coordinate Transformation

Min Yan, Wei Yan, and Min Qiu*

Department of Microelectronics and Applied Physics,

Royal Institute of Technology, Electrum 229, 16440 Kista, Sweden

(Dated: February 6, 2020)

Abstract

Cylinder-shaped perfect lens deduced from the coordinate transformation method is proposed. The previously reported perfect slab lens is noticed to be a limiting form of the cylindrical lens when the inner radius approaches infinite with respect to the lens thickness. Connaturality between a cylindrical lens and a slab lens is affirmed by comparing their eigen-field transfer functions. We numerically confirm the subwavelength focusing capability of such a cylindrical lens with consideration of material imperfection. Compared to a slab lens, a cylindrical lens has several advantages, including finiteness in structure, and ability in lensing with magnification or demagnification. Immediate applications of such a cylindrical lens can be in high-resolution imaging and lithography technologies. In addition, its invisibility property suggests that it may be valuable for non-invasive electromagnetic probing.

PACS numbers: 41.20.-q, 42.79.Bh, 42.25.Bs

*Electronic address: min@kth.se

The recent works on invisibility cloaking devices [1, 2] have triggered a widespread interest on design of functioning electromagnetic (EM) devices based on the coordinate transformation approach. In an effort to unify a range of EM “meta-phenomena”, Leonhardt and Philbin point out that a perfect slab lens made of negative index material (NIM) [3] can be interpreted as a result of a coordinate transformation that maps a single region in virtual EM space to multiple regions in physical space [4]. A recent extension of this concept for designing slab lenses with additional operation functions, such as image translation, rotation, and magnification etc, has been presented in [5]. In this paper we report deployment of a spatial mapping in cylindrical coordinate for designing an annular structure which can be considered as a cylindrical analogue of the previously much debated perfect slab lens. Such a cylindrical lens overcomes two shortcomings of a slab lens. Firstly, it has a finite body size. No structural truncation is necessary for its physical implementation[6]. Secondly, it can form magnified or demagnified image. These advantages can make such a lens more favourable across many scenarios. It should be noticed that Pendry has previously proposed a version of perfect cylindrical lens which is based on rolling up a perfect slab lens existing in the virtual EM space [7]. However, some material parameters of Pendry’s cylindrical lens are gradient over the entire domain; in addition, the gradient parameters approach infinity in the interior of the lens. Hence, a direct forward theoretical confirmation of that lens is seemingly impossible, not to mention the difficulty in its realization. In contrast, the cylindrical lens under current study has all finite material parameters, and an appropriate design can leave the exterior region unaltered as free space. Therefore, the final device is much more favourable from both realization and application points of view.

The proposed cylindrical perfect lens is realized by taking a coordinate transformation from a virtual free EM space (r', θ', z') to the physical space (r, θ, z) , both denoted in cylindrical coordinate. To achieve imaging in radial direction, we map the coordinates as $r' = f(r)$, $\theta' = \theta$ and $z' = z$. One simple example of $f(r)$, as illustrated in Fig. 1(a), takes the form of

$$r' = \begin{cases} \frac{sa+(1-s)b}{a}r, & \text{if } r < a; \\ sr + (1-s)b, & \text{if } a \leq r \leq b; \\ r, & \text{if } r > b, \end{cases} \quad (1)$$

where a and b are the inner and outer radii of the deduced cylindrical lens (hence thickness

$d = b - a$), and s is the negative slope deployed in the mapping function. The continuity of the radial mapping function is required in order to achieve impedance-matched material interfaces. The negative slope at $a < r < b$ is responsible for transforming a single region in virtual space to multiple regions in physical space. Whilst the slope can be of any negative value, in this paper we focus mainly on a slope of $s = -1$. In Eq. 1, the space outside the lens body is kept unaltered, which allows the lens structure to work in a free space environment.

Coordinate transformation projects field in EM space directly to physical space in accordance to the form-invariance property of the Maxwell equations. Consider a line current source which is positioned at $r' = \frac{3b-a}{2}$ and oriented along z' axis in virtual space. Its electric radiation field $E'_{z'}$ (a zeroth-order Hankel function) can be mapped to the physical space via the relation $E_z(r) = E'_{z'}(r')$. The resulted field distribution in physical space, illustrated in Fig. 1(b) by its real part, shows as if there are three current sources located at $r = \frac{3b-a}{2}$ (outside), $r = \frac{a+b}{2}$ (within), and $r = \frac{3ab-a^2}{4b-2a}$ (inside). The equivalence of such multiple points in physical space implies that the device is able to duplicate perfect copies of a source [4, 8]. The lens can image either in inward mode (object is placed outside and its image is formed inside) or reversely in outward mode with comparable performances. Given the mapping function described by Eq. 1, the object needs to be placed within a certain distance to the lens' outer surface: outside the lens, the effective region is $b < r_o \leq (2b - a)$; and inside $\frac{ab}{2b-a} \leq r_o < a$.

The mapping function in Eq. 1 can be readily used to understand the so-called hyperlenses proposed in [9, 10, 11] under the context of cylindrical structure. These designs were proposed to solve the impedance mismatch problem of the multilayered cylindrical lenses theoretically analyzed in [12, 13] and demonstrated in [14, 15]. Under the framework of transformation optics, the designs in [9, 10, 11] are inherently “less perfect” than the cylindrical lens proposed in this study. The design method proposed in [9] can be interpreted as using an identical mapping function as in Eq. 1, but with a zero slope for $a < r < b$. For such a lens, perfect imaging happens only when the object is placed exactly at $r = a$, and a corresponding image at $r = b$. Notice also that a coordinate transformation with a zero-sloped mapping function leads to unphysical extreme material parameters. While in [10], the design of a hyperlens can again be interpreted as using Eq. 1 but with a close-to-zero positive slope for $a < r < b$. No perfect imaging can be achieved in this scenario. The lens

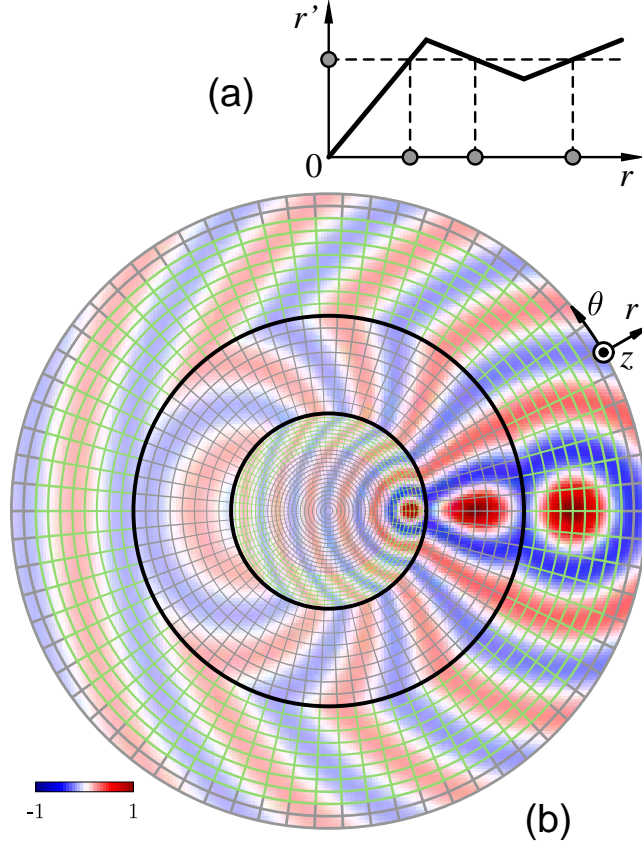


FIG. 1: Schematic illustration of the principle for idealized perfect cylindrical lensing. (a) Spatial mapping function. (b) Imaging of a line current source by a perfect cylindrical lens. Colormap shows the real part of the E_z field.

relays an object's near field at $r = a$ to $r = b$ with minimal decaying, owing to the adjacency of $r = a$ and $r = b$ surfaces in virtual space.

According to the coordinate transformation described by Eq. 1, we derive material parameters for the designed cylindrical lens body ($a \leq r \leq b$) as

$$\epsilon_r = \mu_r = \frac{r - 2b}{r}, \epsilon_\theta = \mu_\theta = \frac{r}{r - 2b}, \epsilon_z = \mu_z = \frac{r - 2b}{r}, \quad (2)$$

and for interior region $r < a$ as

$$\epsilon_r = \mu_r = 1, \epsilon_\theta = \mu_\theta = 1, \epsilon_z = \mu_z = \left(\frac{2b - a}{a} \right)^2. \quad (3)$$

The lens has negative anisotropic permittivities and permeabilities. At $r = b$, the lens has all material parameters valued at -1 , which is perfectly matched to air; at $r = a$, it has $\epsilon_r = \mu_r = \frac{a-2b}{a}$, $\epsilon_\theta = \mu_\theta = \frac{a}{a-2b}$, and $\epsilon_z = \mu_z = \frac{a-2b}{a}$, which matches to the interior material.

EM field in the interior region is compressed in wavelength as compared to in free space due to its larger ϵ_z and μ_z values. This contributes to image demagnification for inward lensing operation, or magnification vice versa. It is worth mentioning that when the lens thickness d is very small compared to a , the lens' material parameters at $r = a$ approach to -1 , whereas ϵ_z and μ_z values of the interior material approach to 1. That is, the cylindrical lens physically becomes a previously reported prefect slab lens [3].

The perfect cylindrical lensing phenomenon predicted by coordinate transformation, as illustrated in Fig. 1(b), however should be verified using full-wave analyses. One factor for the necessity of such explicit verification is that coordinate transformation has presumed the time-harmonic steady state. In a previous time-domain analysis for a slab lens, it was noticed that re-construction of a Fourier field component at the other side of the lens can take impractically long time when the slab index approaches to ideal value, i.e. -1 [16]. This suggests that *perfect* imaging by a slab lens is rather a “wishful” event which relies on infinite happening time. Nevertheless, subwavelength imaging can be realized by slab lenses *with imperfect materials* [16, 17]. Our frequency-domain finite element calculation showed no convergence for a cylindrical lens with ideal parameters as specified by Eq. 2, which reflects the same singular problem of the lens. In the following analyses, we examine the performance of cylindrical lenses with the presence of material perturbations.

For ease of clarification, we restrict our studies to in-plane propagation case (wave vector in $r\theta$ plane) with electric field solely polarized in z direction (E_z polarization). It should however be kept in mind that coordinate transformation promises focusing in a full 3D scenario with arbitrary wave polarization. The relevant material parameters hence are ϵ_z , μ_r , and μ_θ . We append a common factor ϱ , with $\varrho = 1 + \delta$, to each of the lens' ideal material parameters. δ is referred to as material perturbation, and its imaginary part represents material loss. Material perturbation, especially loss, is inevitable for resonance-based negative permittivity or permeability metamaterials. For convenience, we denote layers in the three-layered system from inside to outside as layer 1, 2 and 3 respectively. General field

solutions in three layers, in terms of E_z , are

$$E_z^1 = \sum_m \left\{ \mathcal{A}_m^1 J_m \left(k_0 \frac{2b-a}{a} r \right) + \mathcal{B}_m^1 H_m^{(1)} \left(k_0 \frac{2b-a}{a} r \right) \right\} \exp(im\theta), \quad (4)$$

$$E_z^2 = \sum_m \left\{ \mathcal{A}_m^2 J_m(k_0 \varrho(r-2b)) + \mathcal{B}_m^2 H_m^{(1)}(k_0 \varrho(r-2b)) \right\} \exp(im\theta), \quad (5)$$

$$E_z^3 = \sum_m \left\{ \mathcal{A}_m^3 J_m(k_0 r) + \mathcal{B}_m^3 H_m^{(1)}(k_0 r) \right\} \exp(im\theta), \quad (6)$$

where k_0 is free-space wave number, m is the azimuthal momentum number, and \mathcal{A}^i and \mathcal{B}^i ($i = 1, 2, 3$) are coefficients. We take $\exp(-j\omega t)$ time harmonic dependence. Therefore the Hankel function of the first kind $H_m^{(1)}$ in Eqs. 4-6 represents an outgoing cylindrical wave. Unlike in a planar system where purely evanescent or propagating eigenwaves exist, all eigenwaves in the cylindrical lens system are propagating. Despite the dissimilarity in eigenwaves, we show in the following that superlensing mechanisms of two types of lens can be bridged.

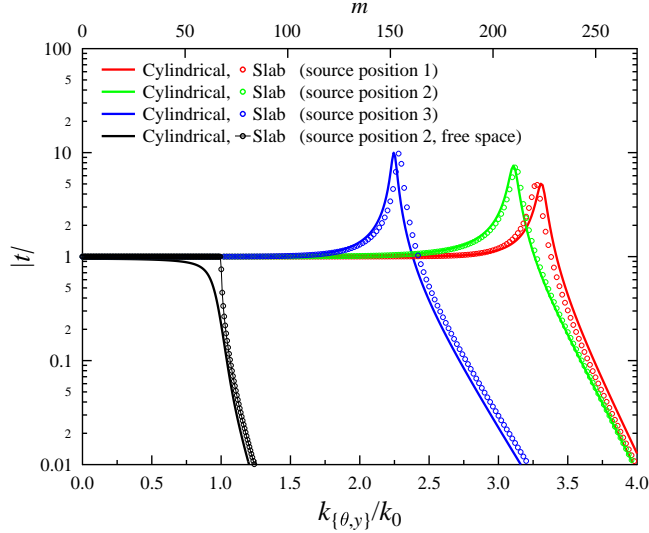


FIG. 2: Comparison of transfer functions for a cylindrical lens and a slab lens of the same thickness.

Three different object positions are shown: for cylindrical lens $r_{o,1} = \frac{5ab-a^2}{8b-4a}$, $r_{o,2} = \frac{3ab-a^2}{4b-2a}$, $r_{o,3} = \frac{7ab-3a^2}{8b-4a}$; and for slab lens $x_{o,1} = -\frac{5d}{4}$, $x_{o,2} = -d$, $x_{o,3} = -\frac{3d}{4}$. Two sets of object positions are equivalent when a and b are much larger than d . For the cylindrical lens the corresponding angular momentum number is marked on the secondary x axis.

First, we consider a cylindrical lens whose inner radius a is much greater than both its thickness d and the operating wavelength. The system resembles a slab lens in both

geometry and material parameters. Our objective is to show how the imaging performances of such a cylindrical lens and a slab lens of the same thickness can be quantified in a unified manner. For a slab lens, the transfer function, which describes the ratio of field strengths at image and source positions for each plane wave component, has been used for describing its imaging capability [16, 17, 18]. Consider a slab lens with thickness $d = \lambda/2$ which is placed in yz plane and centered at $x = 0$. Likewise, we assume that waves are propagating in xy plane with pure E_z polarization. The slab lens has material parameters of $\epsilon = \mu = -\rho = -1 - \delta$, with $\delta = 0.0001 - 0.00001i$. Its transfer functions, as characterized by normalized k_y are shown in Fig. 2 (solid curves) for three different object positions. For this particular material perturbation introduced, restoration of evanescent waves ($k_y > k_0$) at the image positions (always $2d$ apart from the source) has been realized up to a certain k_y . The transfer functions are characterized by a resonance before the transmission damps heavily. The free-space transfer function from the source position to image position (without the slab lens) is also included in Fig. 2. The evanescent waves can barely reach the image position. For a cylindrical lens, one may first be puzzled by absence of decomposable wavevectors in the general solutions (Eqs. 4-6). In fact, the azimuthal momentum number m determines the pace of field variation along the surface-tangent (θ) direction. The azimuthal momentum number can be converted to azimuthal wave number as $k_\theta = m/r_i$, where r_i is the radial image position [19]. In order to obtain sharp image especially in θ direction, existence of high-order cylindrical wave components *at the image position* is essential. Hence, transmission of cylindrical waves through a cylindrical lens provides vital information for the lens' imaging capability. Here we consider a cylindrical lens with $d = \lambda/2$ and $a = 10\lambda$. δ is kept the same as in the slab case. The cylindrical wave transfer functions for outward lensing operation, plotted in terms of normalized k_θ , are superimposed in Fig. 2. Three different object positions have been studied in Fig. 2. The transfer function records the ratio of field strengths at the image and source positions at different cylindrical wave order number m . For each m , the field ratio is derived through matching of the tangential fields at both $r = a$ and $r = b$ interfaces. Refer to Eqs. 4-6, for outward imaging operation, the task is to find the coefficient \mathcal{B}^3 from a known value of \mathcal{B}^1 ; while for inward imaging operation, the task is to find the coefficient \mathcal{A}^1 from a known value of \mathcal{A}^3 . Unlike for a slab lens case, the transfer function for a cylindrical lens is too lengthy to be expressed here owing to the presence of transcendental Bessel functions. For consistency, the free-space cylindrical

wave transfer function is also shown. From Fig. 2, we notice excellent agreement between the transfer functions for cylindrical and slab lenses. With the same thickness and material perturbation, the two types of lenses are therefore equivalent in their imaging capabilities. Both of them can restore a spectrum of waves ($k_{\{\theta,y\}} > 1$) that were lost in the absence of the lenses. Figure 2 provides independent verification of the sub-wavelength imaging capability of a cylindrical lens.

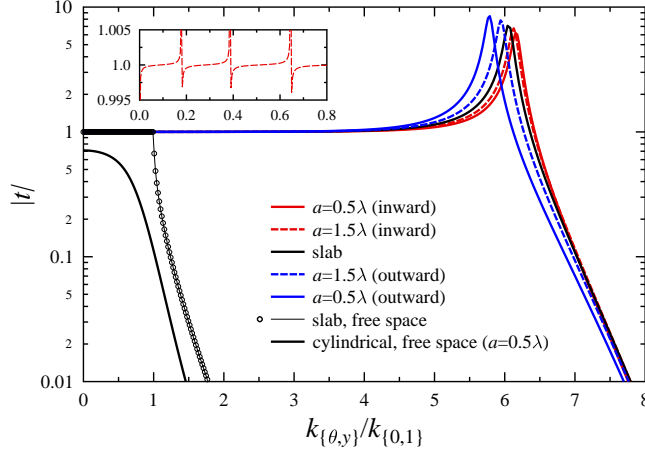


FIG. 3: Effect of a on cylindrical wave transfer function. Inset gives the zoom-in view of the transfer function with $a = 1.5\lambda$ (inward).

Next, we look into the imaging performance of a cylindrical lens as its inner radius a decreases. At a smaller a value, the physical problem becomes more distinct as compared to a slab lens. It is worth noting that, when the object and image points under examination are very close to the origin of cylindrical system, a cylindrical wave can appear to be a strong mixture of both propagating and evanescent waves. This can be observed by comparing the free-space transfer functions in slab and cylindrical systems shown in Fig. 3. Having known this, one would naturally expect to see the distinct character of a cylindrical lens as reflected in its transfer function. The result however turns out to be a bit surprising. The cylindrical wave transfer function is hardly affected when its inner radius is reduced even close to wavelength. In our case study, we fix thickness $d = 0.25\lambda$ and decrease a from infinity to 0.5λ . Material perturbation is again held at $\delta = 0.0001 - 0.00001i$. Besides showing the effect of reducing a on the transfer function, we also take this opportunity to examine the difference in performances between two operation modes of the same lens, i.e. inward imaging and outward imaging. For each operation mode, we start from the slab

lens case ($a = \infty$), and decrease a to 1.5λ and then to 0.5λ . The variation of the transfer function is shown in Fig. 3. Notice that for inward operation, k_θ is normalized with respect to the wavenumber in layer 1, i.e. $k_1 = k_0 \frac{2b-a}{a}$. Object position for inward operation is at $(3b - a)/2$, and for outward operation $(3ab - a^2)/4b - 2a$. Figure 3 shows that the transfer function shifts only very slightly when a decreases from infinity to 0.5λ . Therefore it can be concluded that, with the same thickness and material perturbation, a cylindrical lens, even at an overall scale comparable to wavelength, is as effective as a slab lens for achieving subwavelength imaging. The sharp variations of the inward transfer functions at small k_θ values (see the inset in Fig. 3) are due to near zero field values at both object and image positions. They are not caused by resonances.

The inevitable material imperfectness imposes a rather stringent limitation on the lens shell thickness. For a slab lens, it has been noticed that a smaller thickness drastically improves the imaging performance (or equivalently, relaxes the requirement for material perfectness in order to achieve the same subwavelength imaging) [17]. We have noticed the same for cylindrical lenses. This information can be obtained by comparing Fig. 2 and Fig. 3. In general, with a reasonable material perturbation, the thickness of a cylindrical lens should be kept less than a wavelength in order to achieve subwavelength resolution. Here we fix $d = 0.25\lambda$ and focus on the effect of material perturbation on the cylindrical superlensing performance. We first examine the effect of material loss by keeping the real part of δ , or $\Re(\delta)$, at 0.0001, and increasing the imaginary part $\Im(\delta)$ from 0.00001 up to 0.001. The variation of the transfer function is shown in Fig. 4. From the figure, it is noticed that if $\Im(\delta) < \Re(\delta)$, only the “finess” of the resonance peak is affected. Higher loss suppresses the resonance. Only when $\Im(\delta) > \Re(\delta)$, the transmission starts to drop at a significantly lower k_θ value, which therefore affects the image resolution. A material perturbation dominated by either its real part or imaginary part (but with around the same value) will result in similar transfer functions, with the exception that no resonance peak is present for the transfer function resulted from the latter perturbation. This is confirmed by two curves ($\delta = 0.0001 - 0.001i$ and $\delta = 0.001 - 0.0001i$) in Fig. 4. The imaging enhancement factor, defined as the maximum k_θ/k_1 at which the transmission from the object to image is close to unity is about 4.5 for $\delta = 0.0001 - 0.001i$ and 6 for $\delta = 0.0001 - 0.00001i$. The results suggest that cylindrical lenses under study are able to image with subwavelength resolution. When the perturbation is reduced further, the resonance peak will shift to a even larger k_θ

value. In the limit, for an ideal lens the resonance happens at infinite k_θ .

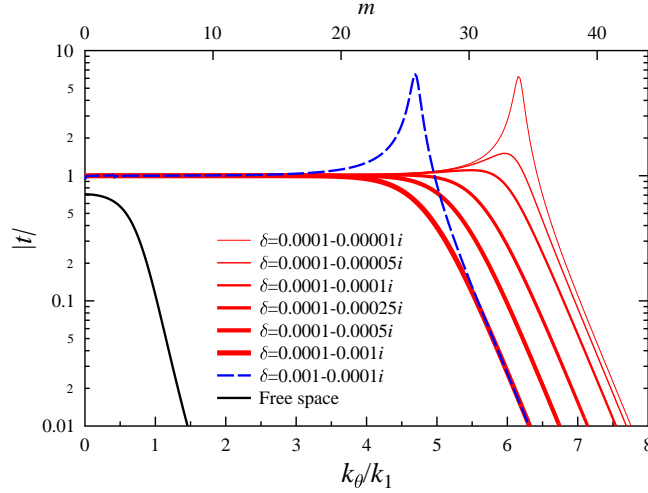


FIG. 4: Effect of δ on cylindrical wave transfer function. Azimuthal momentum number is marked on the secondary x axis.

In Fig. 5, we show the radial $|E_z|$ field distribution of a high-order cylindrical wave ($m = 15$) for the lens studied in Fig. 4. Particularly, we increase the loss perturbation and observe its effect on field profile. $\Re(\delta)$ is kept at 0.0001, and $\Im(\delta)$ is changed from 0.00001 to 0.005, 0.05, and 0.1. The study is for inward imaging scenario. The cylindrical wave, at the vicinity of the object or image position, resembles a purely evanescent wave. The field only becomes oscillating at a distance further away from the origin. With a very small loss, the incoming field from outside penetrates freely (through the formation of a so-called anti surface mode at the outer interface) into the lens body and excites a surface mode at the inner lens boundary. The field amplitude is therefore amplified. With a further decay in lens interior, the field amplitude at the image position is almost exactly the same as at the object position. Restoration of the cylindrical wave is realized. When the loss increases, a surface mode starts to build up at the outer boundary of the lens, while the strength of the surface mode at the inner boundary is gradually muted. At $\Im(\delta) = 0.01$, the loss becomes so heavy that the first surface mode also weakens. The results shown here are very similar to those noticed for a slab lens [20].

To compliment the above transfer function analyses, here we numerically demonstrate the imaging performance of cylindrical lenses using the finite element method (FEM). The issue of coupled surface-mode resonance, which gives rise to the peaks in the transfer functions, is

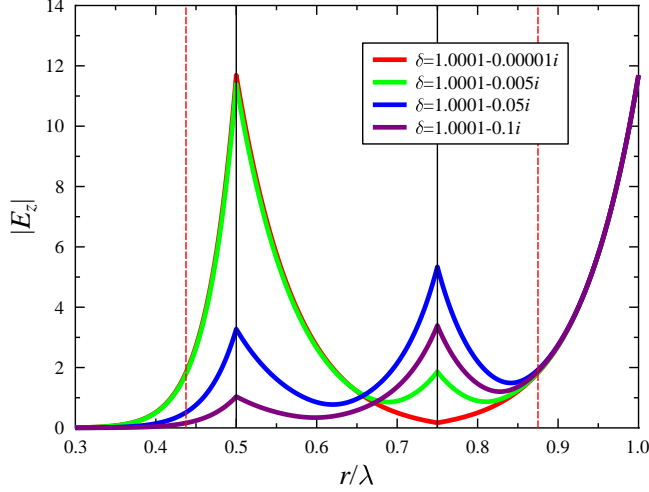


FIG. 5: Radial $|E_z|$ field distributions as material loss increases. The vertical solid black lines denote lens boundaries; dashed red lines denote object and image positions.

also addressed here. The first lens to be examined has parameters of $a = 0.5\lambda$ and $d = 0.25\lambda$, and $\delta = 0.0001 - 0.00001i$. We position a z -oriented line current source at $r_o = (3b - a)/2$. An image is expected at $r_i = (3ab - a^2)/(4b - 2a)$ in lens interior. The real part of the steady state $|E_z|$ field is captured in Fig. 6(a). An image is clearly re-constructed inside the lens. However, the most noticeable difference as compared to the idealized field distribution in Fig. 1 is that strong localized fields are present at the two surfaces of the lens. The maximum field values on the surfaces are as high as 6500 positively and -5000 negatively (in arbitrary unit), which are about 10 times as large as the value at the object position. There are altogether 70 nodal lines along azimuthal direction, indicating the resonance happens around $m = 35$, which agrees with its corresponding transfer function in Fig. 2. The imaginary part of the field (not shown) has the same number of nodal lines, but with different positions as compared to the real part. Hence the surface wave is not standing, but traveling along θ direction. An examination of the Poynting vector plot confirms giant energy flow around the lens' surfaces (not shown). The huge amount of energy that the lens can trap suggests that it may require a certain amount of time for the system to reach its steady state, and in turn to form the image. Another consequence of the existence of heavy surface modes is that it may disallows an object from being placed very near or very far to the lens surface, which adds further restriction on the effective lensing and detecting areas. From Fig. 4, we know that a relatively lossy material can help to suppress the resonance peak in transfer

function, though at the expense of a lower achievable resolution. We therefore carried out another FEM analysis for the same structure but with $\delta = 0.0001 - 0.001i$. The real part of the E_z field is shown in Fig. 6(b). Compared to Fig. 6(a), complete suppression of the surface mode is seen at surface positions away from the line source. Still, surface mode is present close to the line source, but its strength has been reduced considerably compared to the previous calculation. For both cases, despite the localized surface modes, field *outside the lens* experiences almost no disturbance by the lens structure; it appears to be radiated directly from the line source. Therefore the lenses are almost invisible to an observer. The invisibility is due to the fact that the particular coordinate transformation deployed assures the whole structure bounded by $r < b$ is electromagnetically equivalent to vacuum. The perturbations introduced here are insignificant for affecting the invisibility property.

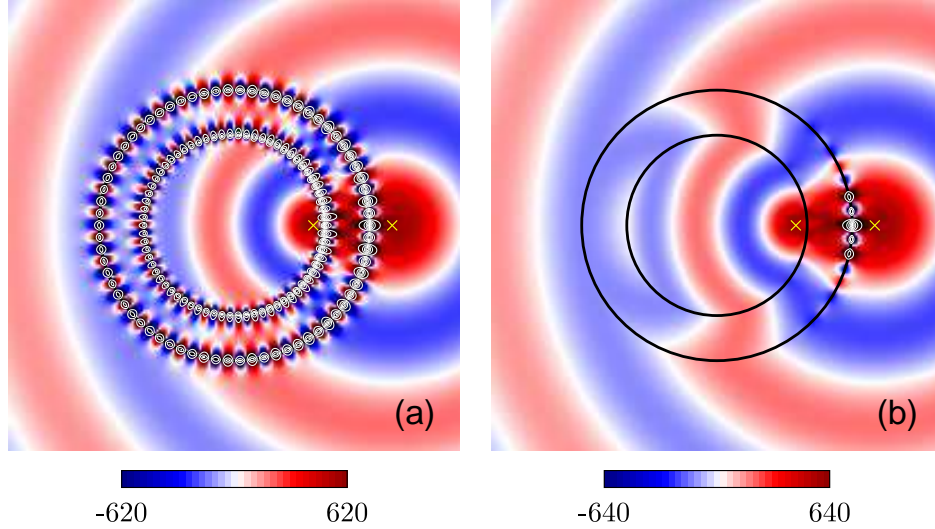


FIG. 6: Inward imaging of a line current source. (a) $\delta = 0.0001 - 0.00001i$. Overvalued field are shown in saturated color as dark red (positive) or dark blue (negative), and contour lines at the levels of ± 1000 , ± 2000 , ± 3000 , ± 4000 , ± 5000 and 6000 are marked. (b) $\delta = 0.0001 - 0.001i$. Contour lines at the levels of ± 1000 , ± 1500 , 2000 , 2500 , 3000 and 3500 are marked. Yellow crosses are object and image positions. Domain size: $2.5\lambda \times 2.5\lambda$.

With the same two lenses, we numerically demonstrate their inward imaging of two parallel line current sources. Such numerical experiments provide direct evidence for the maximum achievable resolution. Note that here we calculate the distance between two line sources or their images by considering they are located on a cylindrical plane (concentric to

the lens surfaces). Two z -oriented line sources are placed at $r_o = (3b - a)/2$, and azimuthally separated by a distance denoted as ΔL_θ . Their images are recorded while ΔL_θ is decreased gradually. The recorded electric field intensity at object and image planes for the low-loss and lossy lenses are shown by the panels in the first and second rows in Fig. 7, respectively. For the low-loss lens, the intensity at the image plane shows very clearly the presence of two peaks when $\Delta L_\theta = 0.22\lambda$, which corresponds well to the field at the object plane. As ΔL_θ decreases, the peaks become less evident, and they are overtaken by a central intensity peak when $\Delta L_\theta = 0.16\lambda$. The central peak is caused by the extension of a strong surface mode. It is however arguable that from the image obtained for $\Delta L_\theta = 0.16\lambda$, one still can tell the information of two line sources. The overall image, though distorted, can possibly be corrected through signal processing techniques, especially if one has the preknowledge of the distortion. For the lossy lens, the information of the two current sources is almost completely lost at $\Delta L_\theta = 0.16\lambda$. However, the two line sources becomes identifiable once ΔL_θ reaches 0.18λ . The recorded field intensities show much less ripples due to the suppression of surface modes. In all panels in Fig. 7, the blue curves represent the field intensities at the object and image planes while the lens is absent. Drastic decay in amplitude is noticed for the images recorded without a lens. Hence the restoration of evanescent EM wave by a cylindrical lens is obvious. Comparing the low-loss lens to the lossy one, we notice that the latter suffers less disturbance from surface mode. Due to this factor, its maximum achievable resolutions for both lenses are almost comparable.

Lastly, we comment on the effect of negative slope value used for the spatial mapping function (Eq. 1). In practice, one desires to image an object that is far away from the lens, rather than maneuvering the lens very close to the object for performing an imaging. Theoretically this can be achieved by an increase (negatively) in the negative slope value for the mapping function. However, for a fixed lens thickness, an increase in the slope compresses the field in the lens body, or equivalently increases proportionally the optical lengths for all cylindrical wave components as they travel across the lens body. That unfortunately amplifies the adverse effect of material loss to the lens' performance. We noticed that in order to achieve the same resolution, the thickness of a lens should be kept inversely proportional to the negative slope, assuming the same material perturbation. Due to the necessity of a decrease in lens thickness for maintaining resolution, the object-to-image distance in fact shortens when the negative slope increases. Another note is that an increase in the negative

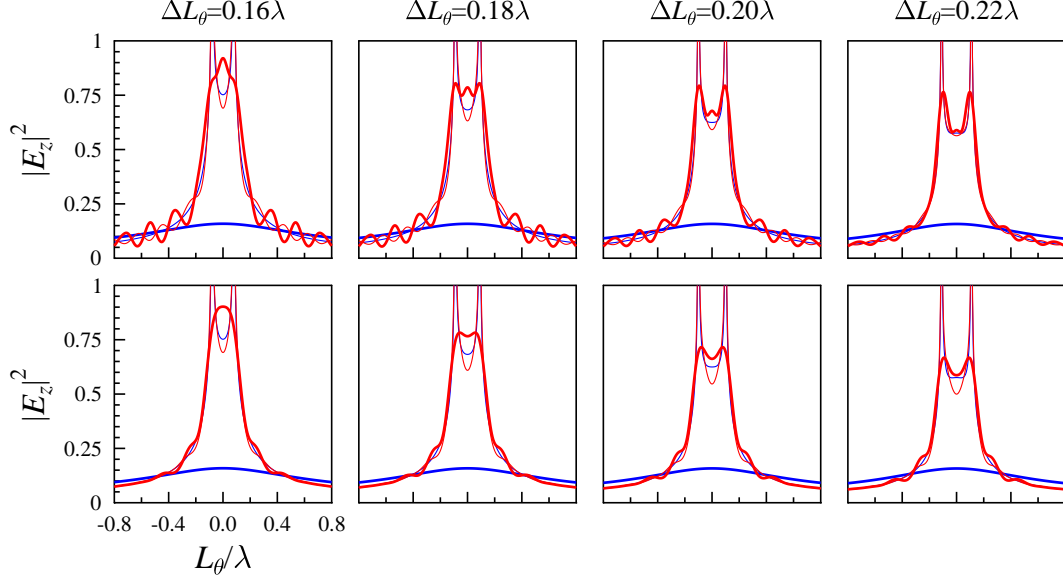


FIG. 7: Imaging of two parallel line current sources. Panels in the first row are for the lens with $\delta = 0.0001 - 0.00001i$, and those in the second row are for the lens with $\delta = 0.0001 - 0.001i$. For panels in both rows, from left to right, ΔL_θ values are respectively 0.16λ , 0.18λ , 0.20λ , and 0.22λ . Notice that the image has been stretched by a factor of $(2b - a)/a$ due to the higher permittivity inside the lens. Red lines: with lens; blue lines: without lens. Thick lines: intensity at image plane; thin lines: intensity at object plane.

slope gives rise to gradient lens material with higher anisotropic ratio. Therefore such a way of increasing the object distance outside the lens is not encouraged.

In conclusion, based on the coordinate transformation technique we have designed a type of cylindrical superlenses. The transfer function analyses show that such a cylindrical lens, even with a wavelength-scale cross-section size, can achieve similar subwavelength imaging resolution as compared to the previously reported negative index slab lens. Subwavelength imaging is demonstrated numerically for cylindrical lenses with imperfect material parameters. Like its slab lens counterpart, the cylindrical lens experiences similar limitation as imposed by inevitable material imperfectness. Most noticeably, at a practical loss level, a cylindrical lens should have a subwavelength thickness in order to realize subwavelength focusing. Therefore, these cylindrical lenses are not likely perform well for imaging across a far distance; i.e., they are near-sighted, a conclusion previously drawn for slab lens [18]. Besides high-resolution imaging, the proposed cylindrical lens can be applied for lithography

applications. Consider a single E_z polarization operation. A properly designed cylindrical lens can embed in its interior a dielectric material with perfect impedance matching. Image can then be written on the surface of that dielectric material. The invisibility property of the cylindrical device can also be deployed for non-invasive electromagnetic probing. Although not analyzed in this paper explicitly, the coordinate transformation predicts that the same radial transformation as described in Eq. 1 will yield a spherical superlens. With the current fast-developing metamaterial technology, which has already been used for demonstrating negative refraction [21, 22], subwavelength imaging [14, 15, 23], and even conceptual electromagnetic cloaking [24](also devised in [25] for operating at optical wavelength) etc, we should be able realize fabrication of the proposed cylindrical superlens in near future.

Acknowledgement: This work is supported by the Swedish Foundation for Strategic Research (SSF) through the Future Research Leader program, the SSF Strategic Research Center in Photonics, and the Swedish Research Council (VR).

-
- [1] U. Leonhardt, Science **312**, 1777 (2006).
 - [2] J. B. Pendry, D. Schurig, and D. R. Smith, Science **312**, 1780 (2006).
 - [3] J. B. Pendry, Phys. Rev. Lett. **85**, 3966 (2000).
 - [4] U. Leonhardt and T. G. Philbin, New J. Phys. **8**, 247 (2006).
 - [5] D. Schurig, J. B. Pendry, and D. R. Smith, Opt. Express **15**, 14772 (2007).
 - [6] The adverse effect of inevitable truncation for a slab lens to its imaging performance is studied in L. Chen, S. He, and L. Shen, Phys. Rev. Lett. **92**, 107404 (2004).
 - [7] J. B. Pendry, Opt. Express **11**, 755 (2003).
 - [8] More generally speaking, the cylindrical annular structure perfectly duplicates within its enclosed region the EM events happening outside the cylinder, or vice versa.
 - [9] M. Tsang and D. Psaltis, Phys. Rev. B **77**, 035122 (2008).
 - [10] A. V. Kildishev and E. E. Narimanov, Opt. Lett. **32**, 3432 (2007).
 - [11] A. V. Kildishev and V. M. Shalaev, Opt. Lett. **33**, 43 (2008).
 - [12] A. Salandrino and N. Engheta, Phys. Rev. B **74**, 075103 (2006).
 - [13] Z. Jacob, L. V. Alekseyev, and E. Narimanov, Opt. Express **14**, 8247 (2006).

- [14] Z. Liu, H. Lee, Y. Xiong, C. Sun, and X. Zhang, *Science* **315**, 1686 (2007).
- [15] I. I. Smolyaninov, Y.-J. Hung, and C. C. Davis, *Science* **315**, 1699 (2007).
- [16] X. S. Rao and C. K. Ong, *Phys. Rev. E* **68**, 067601 (2003).
- [17] D. R. Smith, D. Schurig, M. Rosenbluth, S. Schultz, S. A. Romakrishna, and J. B. Pendry, *Appl. Phys. Lett.* **82**, 1506 (2003).
- [18] V. A. Podolskiy and E. E. Narimanov, *Opt. Lett.* **30**, 75 (2005).
- [19] Following the argument, the factor $\exp(im\theta)$ in Eqs. 4-6 can be re-configured as $\exp(ik_\theta(m, r)L_\theta(r))$, where $L_\theta = \theta r$ is the azimuthal distance.
- [20] X. S. Rao and C. K. Ong, *Phys. Rev. B* **68**, 113103 (2003).
- [21] R. A. Shelby, D. R. Smith, and S. Schultz, *Science* **292**, 77 (2001).
- [22] S. Zhang, W. Fan, N. C. Panoiu, K. J. Malloy, R. M. Osgood, and S. R. J. Brueck, *Phys. Rev. Lett.* **95**, 137404 (2005).
- [23] N. Fang, H. Lee, C. Sun, and X. Zhang, *Science* **308**, 534 (2005).
- [24] D. Schurig, J. J. Mock, B. J. Justice, S. A. Cummer, J. B. Pendry, A. F. Starr, and D. R. Smith, *Science* **314**, 977 (2006).
- [25] W. Cai, U. K. Chettiar, A. V. Kildishev, and V. M. Shalaev, *Nat. Photonics* **1**, 224 (2007).